Geomechanics and Engineering, *Vol. 12*, *No. 3* (*2017*) *541-560*
DOI: https://doi.org/10.12989/gae.2017.12.3.541

Experimental and numerical study on the fracture coalescence behavior of rock-like materials containing two non-coplanar filled fissures under uniaxial compression

Wen-Ling Tian and Sheng-Qi Yang*

State Key Laboratory for Geomechanics and Deep Underground Engineering, School of Mechanics and Civil Engineering, China University of Mining and Technology, Xuzhou 221116, PR China

(*Received July 18, 2016, Revised October 20, 2016, Accepted November 22, 2016*)

Abstract. In this research, experimental and numerical simulations were adopted to investigate the effects of ligament angle on compressive strength and failure mode of rock-like material specimens containing two non-coplanar filled fissures under uniaxial compression. The experimental results show that with the increase of ligament angle, the compressive strength decreases to a nadir at the ligament angle of 60°, before increasing to the maximum at the ligament angle of 120°, while the elastic modulus is not obviously related to the ligament angle. The shear coalescence type easily occurred when $\alpha < \beta$, although having the same degree difference between the angle of ligament and fissure. Numerical simulations using PFC^{2D} were performed for flawed specimens under uniaxial compression, and the results are in good consistency with the experimental results. By analyzing the crack evolution process and parallel bond force field of rock-like material specimen containing two non-coplanar filled fissures, we can conclude that the coalescence and propagation of crack are mainly derived from parallel bond force, and the crack initiation and propagation also affect the distribution of parallel bond force. Finally, the displacement vectors in ligament region were used to identify the type of coalescence, and the results coincided with that obtained by analyzing parallel bond force field. These experimental and numerical results are expected to improve the understanding of the mechanism of flawed rock engineering structures.

Keywords: rock-like materials; filled fissures; PFC; parallel bond force; crack coalescence

1. Introduction

Rock masses are heterogeneous due to the existence of various types of flaw (such as holes, fissures, inclusions) (Lin *et al*. 2015, Zhang and Wong 2013, Janeiro and Einstien 2010), which have been proved having a significant influence on the stability and safety of engineering rock mass (Sagong and Bobet 2002, Yang *et al*. 2008, Park and Bobet 2009). In the past several decades, many experimental and numerical research efforts have been carried out on rocks under different loading conditions (Lee and Jeon 2011, Bobet and Einstien 1998, Xiao *et al*. 2015, Wang *et al*. 2015, Gehle and Kutter 2003, Haeri *et al*. 2015, Yang 2015, Yang *et al*. 2017).

Prudencio (Prudencio and Jan 2007) carried out biaxial tests on physical models of rock with non-persistent joints, and the results showed that the failure modes and maximum strength

*Corresponding author, Professor, E-mail: yangsqi@hotmail.com

http://www.techno-press.org/?journal=gae&subpage=7 ISSN: 2005-307X (Print), 2092-6219 (Online)

developing rules depended on the geometry of joint systems, the orientation of principal stresses, and the ratio between intermediate stress and intact material compressive strength. Then, Bahaaddini (Bahaaddini *et al*. 2013) used PFC^{3D} to investigate the effects of geometric parameters of joints on the rock mass failure mechanism, unconfined compressive strength and deformation modulus. Wong (Wong and Einstein 2009) characterized the cracks that emanated from a single pre-existing fissure, and identified seven different crack types based on their geometries and mechanisms. Huang (Huang *et al*. 2016) investigated the initiation and propagation of cracks from pre-existing fissures under triaxial compression, and found that the arrangement of the flaw pair has greater impact on rock deformation, strength and crack coalescence pattern than the confining pressure. Gerolymatou (Gerolymatou and Triantafyllidis 2016) carried out an experimental study on a series of gypsum specimens with pre-existing cracks under simple shear pressure, used the hypothesis of averaged cohesion and the theory of fracture to reproduce the results, found that fracture mechanics provided a more suitable model for the experimental results. Haeri (Haeri *et al*. 2015) studied the breakage process of the disk by inserting single and double fissures with different inclination angles, and used numerical simulation to study the effects of crack length and its orientation on crack coalescence and breakage path. Xu (Xu *et al*. 2016) studied the progressive rock fracture mechanism of the CCNBD rock specimen under mixed mode loading by RFPA^{3D}, and the results showed that not only the notch tip but also the saw-cut chevron notch cracks during the experiments, yielding a prominent twisted front, far from being straight.

Work in the past mainly focused on open fissures, but few researches studied filled fissures (Shen *et al*. 1995, Zhang and Wong 2012, Liu and Zhang 2015). In fact, fissures in rock are often filled with sands, ooze and etc. In this research, experimental and numerical simulation were adopted to investigate the effects of ligament angle on compressive strength and failure mode of rock-like material specimen containing two non-coplanar filled fissures under uniaxial compression. First, mica sheet was used as fillings in fissures of rock-like material specimen to produce filled fissures, and investigate the fracture coalescence process of rock-like material containing two non-coplanar filled fissures. And then, PFC^{2D} was used to simulated the flawed specimen under uniaxial, based on the analysis of micro-parameters calibration, crack evolution process, parallel bond force field and displacement vectors in ligament region.

2. Specimens and testing produce

Rock-like materials are widely used in experiments to investigate the mechanical behaviors of the rock containing pre-existing fissures since they are very homogeneous, easy to add the pre-existing fissures or joints. Moreover, it can provide desirable brittleness. In this research, specimens were made of white cement, quartz sand and water, through a great amount of trial and error test, the mass proportions were obtained for all the specimens used in the test that white cement/quartz sand/water = 1: 0.86: 0.45. The white cement used was NO. 32.5, the quartz diameter was between 0.11~0.21 mm, and the water was tap-water. The material mechanical parameters were: Young's modulus E = 5.74 GPa, uniaxial compressive strength σ_c = 43.73 MPa, and Brazilian tensile strength σ_t = 3.45 MPa.

In order to observe the cracks propagation behavior of rock containing pre-existing filled fissures, mica sheet was chosen as the filling material, as shown in Fig. 1(a), the mica sheet of 0.8 mm thickness first knifed to width of 12 mm. And then placed the mica sheet in the grooving of the model, which consists of two side boards and one base board, easy to be reassembled. The

(a) Mica sheet

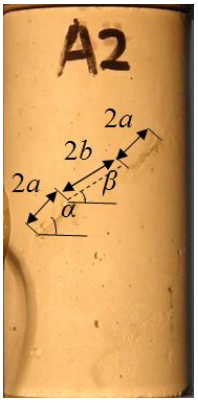

(b) Geometry of two non-coplanar fissures

Fig. 1 The process to make specimens containing pre-existing non-coplanar fissures

mixture was poured into the steel mold, the specimen was unmolded after stored at room temperature for 24 h. The size of the tested specimens was approximately 50×100 mm. The geometry of the specimens with two non-coplanar was described in Fig. 1(b), and it was defined by four geometric parameters: fissure length 2a, ligament length 2b, fissure angle (the angle of the fissure with the horizontal direction) α, and ligament angle β. In this research, different geometries of two non-coplanar fissures were produced by varying the ligament angle from 30~90°, with an interval of 30°, while keeping the other parameters constant (2a = 12 mm, 2b = 16 mm, and α = 45°).

Testing of the specimens was done in uniaxial compression until failure, and the loading was applied in a stepwise process at a constant displacement rate of 0.12 m/s. While the crack evolution process was snapped by a digital video camera. This was a continuous shooting progress, which yielded 25 frames per second in order to ensure clear cracks.

3. Experimental results

3.1 Strength and deformation behavior

Fig. 2 showed the uniaxial stress-strain curve and ultimate failure mode of intact specimen under uniaxial compression. From Fig. 2, it can be clearly seen that the tested rock-like material was a kind brittle marital which typically undergoes axial splitting failure, and a loud failure sound could be heard during the dropping after peak strength. The axial stress-strain curves and ultimate failure mode exhibited similar behavior and showed very good consistency.

Fig. 3 illustrated the axial stress-strain curves of rock-like material specimens containing two non-coplanar filled fissures with different ligament angles under uniaxial compression. From Fig. 3, it can be seen that the ligament has a distinct effect on the strength and deformation behavior of specimens subjected to uniaxial compressive stress. Compared with the Fig. 2(a), the stress-strain curves of specimens containing two non-coplanar filled fissures shown in Fig. 3 revealed several distinct stress drops, which resulted mainly from the initiation or coalescence of new cracks during loading.

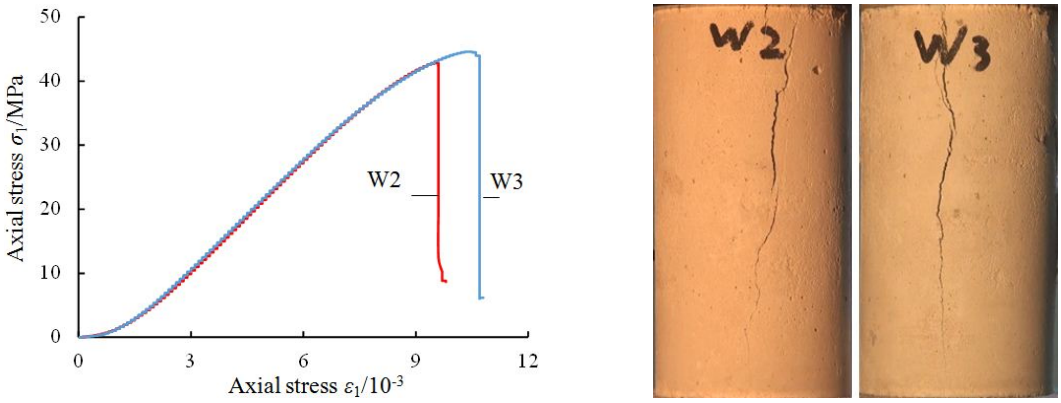

(a) Axial stress-strain curve of intact specimen (b) Ultimate failure mode of intact specimen

Fig. 2 Axial stress-strain curve and ultimate failure mode of intact specimen under uniaxial compression

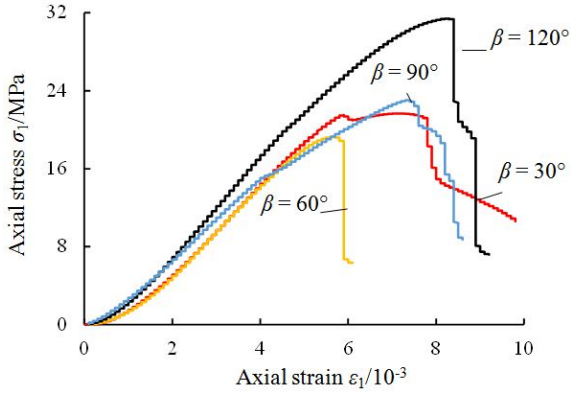

Fig. 3 Axial stress-strain curves of specimens containing filled fissures under uniaxial compression

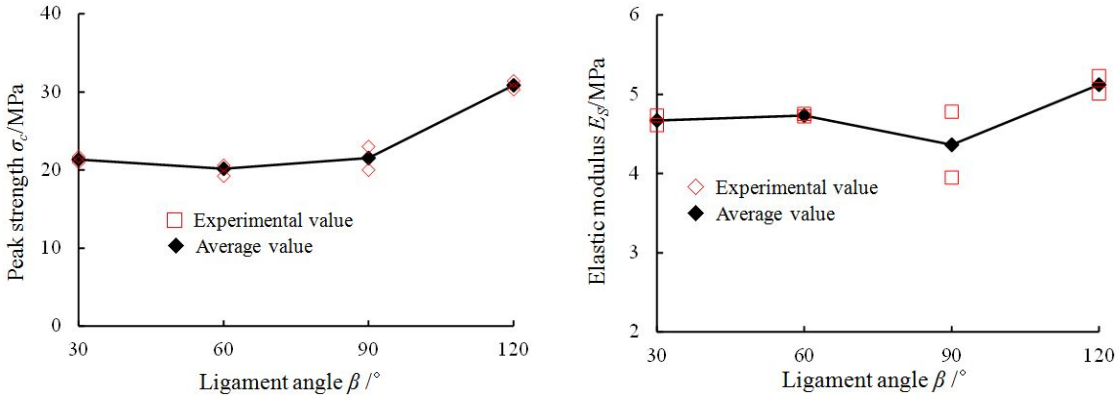

(a) Peak strength (b) Elastic modulus

Fig. 4 Effect of ligament angle on the peak strength and elastic modulus of specimens containing two non-coplanar filled fissures under uniaxial compression

Fig. 4 presented the effects of ligament angle on the mechanical parameters of specimens containing two non-coplanar filled fissures under uniaxial compression. In Fig. 4, σ_c is the peak strength under uniaxial compression, *E*s represents the elastic modulus, i.e., the slop of the approximately linear part between 30~70% of the peak strength of the stress-strain curve. It should be noted that, in the following analysis, the mechanical parameters are the average values of two specimens for the same ligament angle. The results showed that the mechanical parameters of the specimens containing two filled fissures were all lower than those of intact specimens under uniaxial compression. In accordance with Fig. 4(a), it can be seen that the peak strength of specimens containing two filled fissures ranges from 20.18 MPa (β = 60°) to 30.84 MPa (β = 120°). As the ligament angle increased from 30° to 60°, the peak strength decreased from 21.33 MPa to 20.18 MPa, and then the σ_c of flawed specimens increased from 20.18 MPa to 30.84 MPa. The elastic modulus of the flawed specimens ranged from 4.36 GPa to 5.12 GPa, and it was not dependent on the ligament angle.

3.2 Fracture coalescence behavior of specimens containing two non-coplanar filled fissures

Fig. 5 presented the ultimate failure modes of specimens containing two non-coplanar filled fissures under uniaxial compression, and the results differed markedly from that of intact specimens. It can be clearly seen that the ultimate failure modes of specimens were obviously dependent on the ligament angle, and was a mixture of several crack coalescences. So in this section we investigated the crack coalescence in flawed specimens using photographic techniques.

Fig. 6 presented the crack initiation and coalescence process of specimens containing two non-coplanar filled fissures for β = 30°. It can be seen that, before point *a* (σ_1 = 18.99 MPa), the stress concentration at fissure tip did not reach the material strength, consequently did not result in a crack initiation. However when the axial stress was loaded up to point *a*, tensile cracks (cracks $1^{a\sim c}$) initiated from the tip of filled fissure ① and ②, and propagated toward the edge of the specimen along the direction of axial stress, which led the specimen to yield phase.

With increase in the axial deformation, the deformation process from point *a* to *b* (σ_1 = 20.52 MPa), the wing crack 2^a initiated at the inner tip of filled fissure ②, though it was similar to the secondary tensile crack obtained from Yang (Yang and Jing 2011), which initiated along the fissure's direction to some distance and then gradually turned toward the direction of maximum

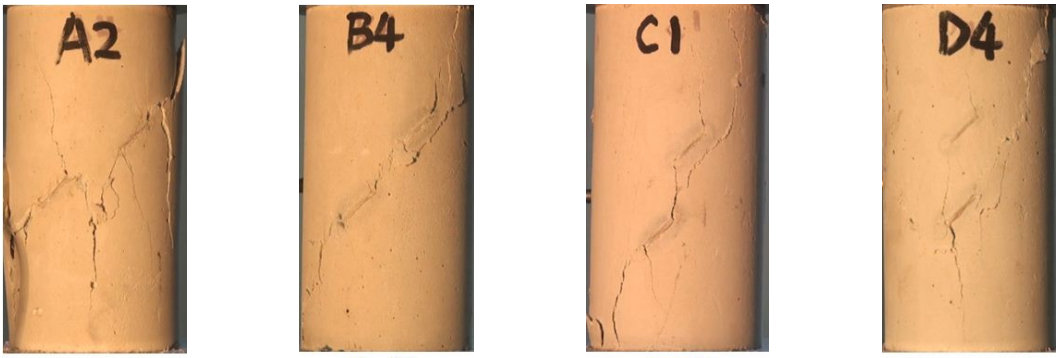

Fig. 5 Ultimate failure modes of rock-material specimen containing two non-coplanar filled fissures

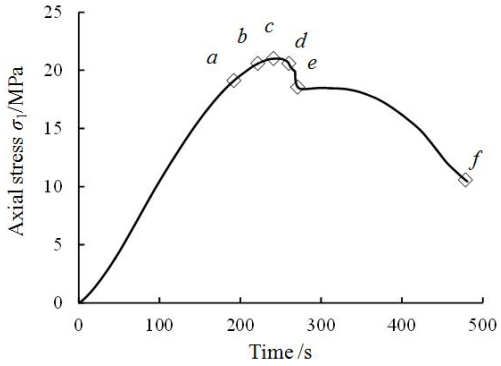

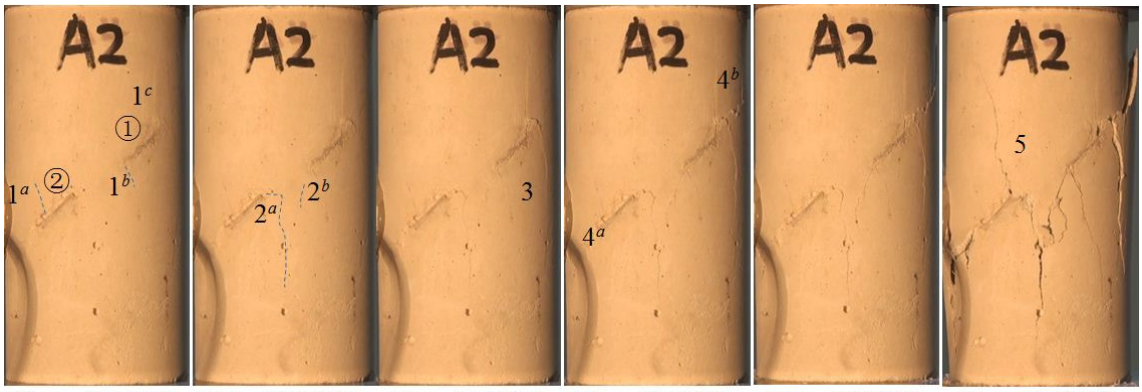

(a) σ_1 = 18.99 MPa (b) σ_1 = 20.52 MPa (c) σ_1 = 21.00 MPa (d) σ_1 = 20.57 MPa (e) σ_1 = 18.90 MPa (f) σ_1 = 10.44 MPa

Fig. 6 Crack initiation and coalescence process of rock-like material specimen containing two non-coplanar filled fissures for $\beta = 30°$

primary stress, while deflecting the opposite orientation. At the same time, shear crack 2^b initiated near inner tip of ①, which was the same as the shear crack observed by Zhuang (Zhuang *et al*. 2014).

When the specimen was loaded to the peak strength (i.e., point *c*), the corresponding axial stress was 21 MPa, the crack 3 emanated from the outer tip of ①, and like the crack 2^a, which initiated along the fissure's direction to some distance and then gradually turned toward the direction of maximum primary stress. Meanwhile, the width of $2^{a\sim b}$ crack increased, but tensile cracks $1^{a\sim c}$ only propagated a little.

After the peak strength, as further increase of axial deformation occurred, the axial stress of the specimen gradually dropped, when dropping to point *d* (σ_1 = 20.57 MPa), the secondary crack $4^{a\sim b}$ initiated and quickly propagated toward the edge of the specimen. Meanwhile, the coalescence occurred between crack 2^b and fissure ①.

The continuous increase of axial deformation led the crack propagated quickly, which led to a bigger stress drop in the axial stress-strain curve, and a loud failure sound could be heard. After dropping to point *e* (σ_1 = 18.90 MPa), the shear $4^{a\sim b}$ cracks had been extended to the edge of the specimen, but the coalescence did not occurred between two fissures, so the specimen also had a certain carrying capacity.

After point *e*, as increase of the axial strain, the axial stress dropped gradually, and finally the

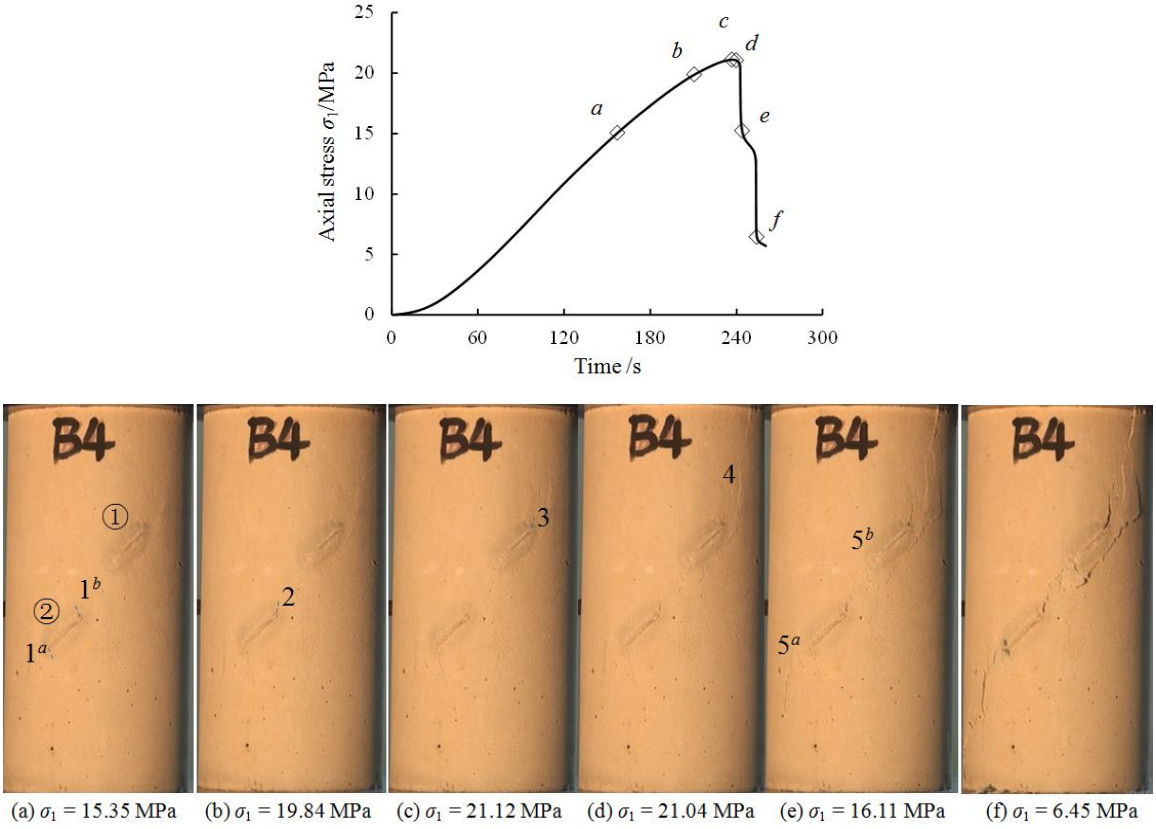

Fig. 7 Crack initiation and coalescence process of rock-like material specimen containing two non-coplanar filled fissures for $\beta = 60°$

coalescence occurred between crack 2^a and 2^b. At the same time, the anti-wing crack 5 initiated at inner tip of fissure ② and propagated toward the edge of specimen, along the direction of the axial stress.

Fig. 7 presented the crack initiation and coalescence process of specimens containing two non-coplanar filled fissures for $\beta = 60°$. When the specimen was loaded to point *a* (σ_1 = 15.35 MPa), two wing cracks $1^{a\sim b}$ initiated from the tip of the fissure ②. With the increase of axial deformation, the stress began to increase slowly.

After reaching point *b*, secondary crack 2 emanated at the inner tip of fissure ②. With the increase of the axial deformation, the specimen was loaded to peak strength, i.e., point *c* (σ_1 = 21.12 MPa), shear crack 3 initiated at outer tip of fissure ①.

Afterwards, axial stress declined gradually. When stress dropped to point *d* (σ_1 = 21.04 MPa), a far-filed crack 4 was observed near outer tip of fissure ①. After point *d*, the axial stress quickly dropped to point *e* (σ_1 = 16.11 MPa) due to serious damage to the supporting structure, the cracks 2~4 propagated quickly. Meanwhile, secondary crack $5^{a\sim b}$ initiated at outer tip of fissure ② and inner tip of fissure ①. When coalescence occurred between two fissures, the specimen destructed completely.

According to Figs. 6 and 7, it can be seen that both of the samples had 15° difference between

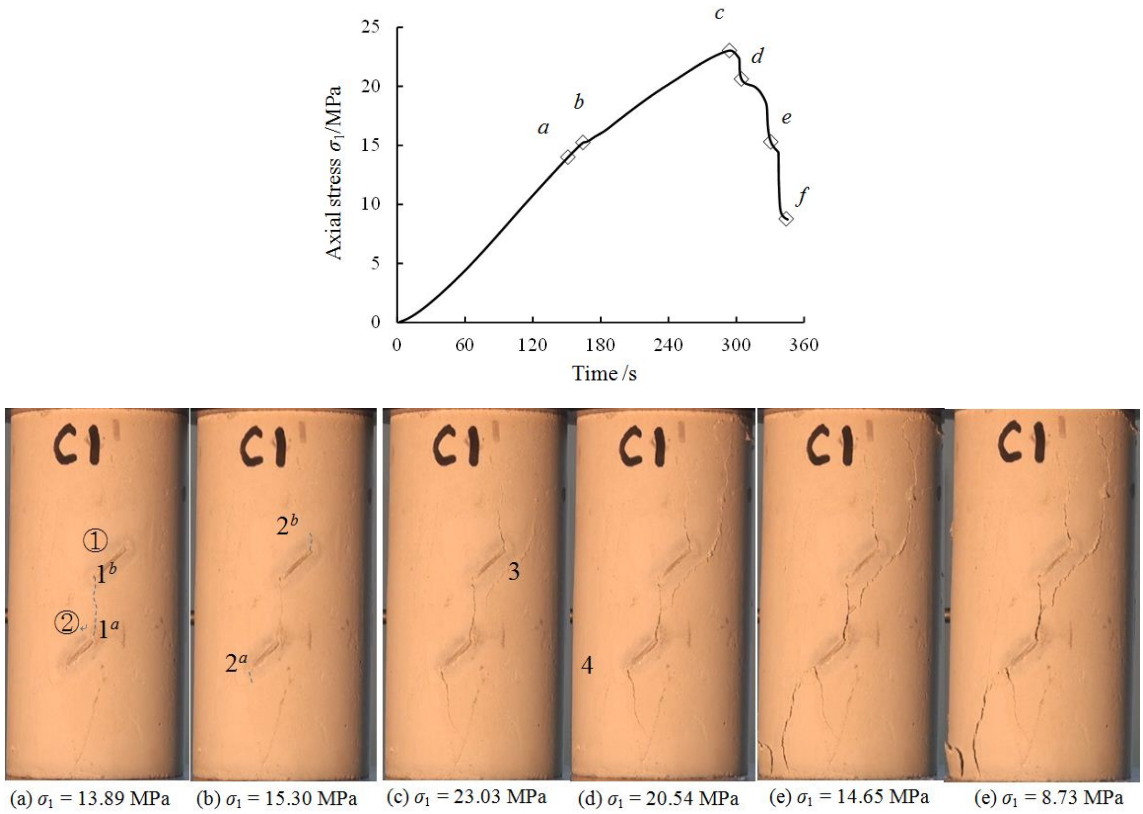

(a) σ_1 = 13.89 MPa (b) σ_1 = 15.30 MPa (c) σ_1 = 23.03 MPa (d) σ_1 = 20.54 MPa (e) σ_1 = 14.65 MPa (e) σ_1 = 8.73 MPa

Fig. 8 Crack initiation and coalescence process of rock-like material specimen containing two non-coplanar filled fissures for $\beta = 90°$

the angle of ligament and fissure, while the coalescence types were quite different, the result agreed with Yang (Yang *et al*. 2016). However, Wong (Wong and Chau 1998) concluded that the shear coalescence mode dominated the strip when slight deviation of either α or β from the line $\alpha = \beta$, while shear type coalescence occurred when $\alpha < \beta$ in this research.

Fig. 8 illustrated the crack initiation and coalescence processes of specimens containing two non-coplanar filled fissures for $\beta = 90°$. When the load was up to point a (σ_1 = 13.89 MPa), wing cracks $1^{a\sim b}$ initiated at inner tip of fissures, and coalescence occurred in the ligament region of specimen. The continuous increase of axial deformation reached point b (σ_1 = 15.30 MPa), two wing cracks 2^a and 2^b emanated from the outer tip of fissures, and at this time, the elastic modulus dropped obviously. When the axial stress loaded up to point c (σ_1 = 23.03 MPa), i.e., peak strength, far-filed crack 3 appeared near the fissure ①, meanwhile cracks 2^a and 2^b propagated along the axial direction.

When the stress dropped to point d (σ_1 = 20.54 MPa), far-file crack 3 propagated to the boundary of the specimen. At the same time, shear crack 4 initiated near the outer tip of fissure ②. Afterward, stress continuously dropped to point e (σ_1 = 14.65 MPa), crack 4 propagated to the boundary of specimen. Finally, stress dropped to point f (σ_1 = 8.73 MPa), and specimen was broken ultimately.

Fig. 9 illustrated the crack initiation and coalescence processes of specimens containing two

non-coplanar filled fissures for $\beta = 120°$. As the figure shown, when the specimen was loaded to point *a* ($\sigma_1 = 18.59$ MPa), wing crack 1^a and 1^b initiated in the outer tip of fissure ② and the inner tip of fissure ①.

After reaching point *b* ($\sigma_1 = 20.10$ MPa) coalescence occurred in ligament region because wing crack 2^a initiated and propagated at the inner tip of fissure ②. When loaded to point *c* ($\sigma_1 = 26.94$ MPa), the anti-tensile crack 3 initiated at outer tip of fissure ②, and propagated along the direction of axial stress.

Later, with the increase of axial deformation, the axial stress began to increase slowly. When the specimen was loaded to the peak strength, i.e., point *d* ($\sigma_1 = 28.35$ MPa), far-file crack 4 initiated near the inner tip of fissure ②. After the peak point, axial stress dropped quickly, when the stress dropped to the point *e* ($\sigma_1 = 10.88$ MPa), anti-wing crack 3 propagated to the inner tip of fissure ①, far-file crack propagated to the boundary of specimen, and coalescence with the fissure ②, and the specimen broke completely.

Through the above analysis, it can be seen that wing crack initiated easily than shear crack. When ligament angle was greater than 60°, the coalescence occurred before the peak strength point, but when ligament angle became smaller than 60°, the coalescence occurred after the peak strength point.

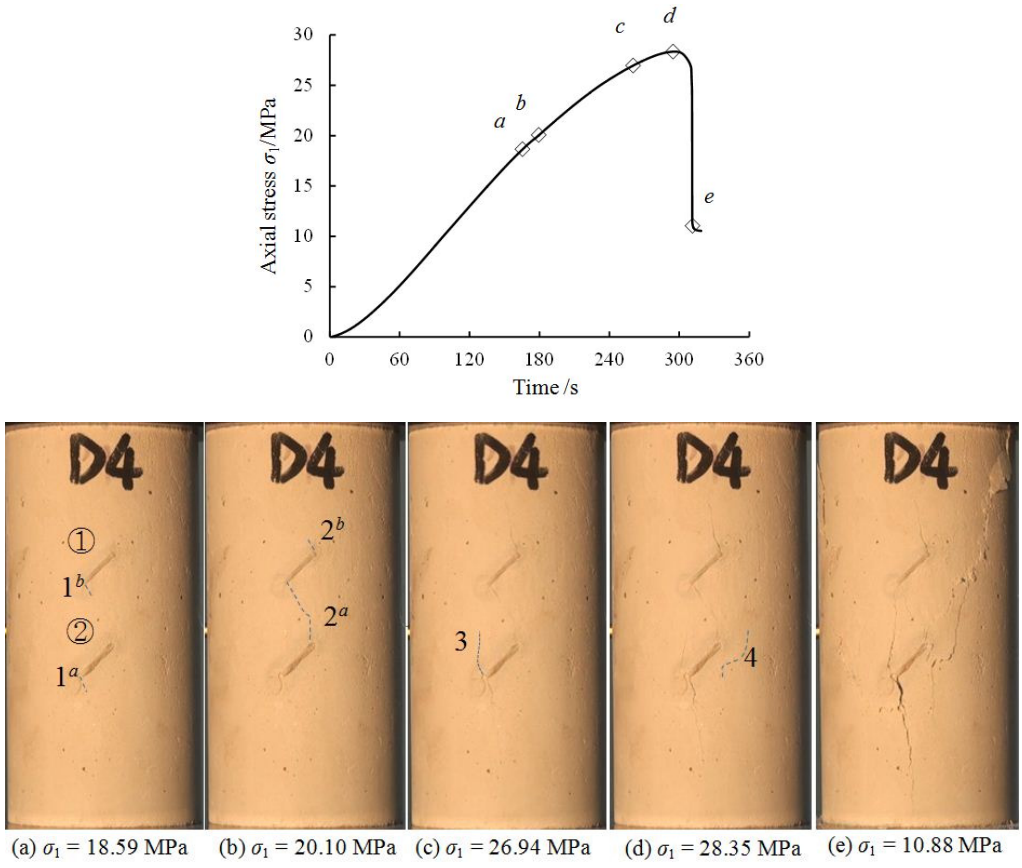

Fig. 9 Crack initiation and coalescence process of rock-like material specimen containing two non-coplanar filled fissures for $\beta = 120°$

4. Numerical modeling and simulated results

4.1 Numerical model and micro-parameters

In this section the two dimension particle flow code was chosen to simulate the crack evolution behavior of specimen containing two non-coplanar filled fissures, Because PFC^{2D} can simulate the crack coalescence behavior of rock material by an assembly of rigid circular particles bonding together at their contact points. First, a numerical intact specimen was generated by PFC^{2D}, and the scale of numerical specimen was similarly equal to that of experimental specimen, i.e., the dimension of 50 mm in width and 100 mm in height. The particle size followed a uniform distribution ranging from 0.2 mm to 0.32 mm, so each numerical specimen was discretized into 22686 particles with 58931 parallel bonds. The average unit weight of rock-like material was about 1768 kg/m^3.

After generating the intact specimen, we created two filled fissures by reset property of the ball, as shown in Fig. 10. As is well-known, it is very difficult to determine micro-parameters by experiments. However, in order to validate the particle properties used in the numerical modeling, it is essential to establish a correlation between the macro-behavior and micro-parameters. During the calibration process, the micro-parameters were confirmed by using the trial and error method (Zhang *et al*. 2012). Because the specimen containing filled fissures has two group micro-parameters: intact specimen's micro-parameters and fissure's micro-parameters, and both micro-parameters influence the peak and ultimate failure mode of flawed specimen mutually. On the base of the numerical stress-strain curve, peak stress and failure mode were similar with the experiment, to ensure the numerical peak strength of flawed specimens had similar trends with the increase of ligament angle through adjusting the micro-parameters of intact specimen. Table 1 listed the micro-parameters used in the PFC^{2D} model for rock-like specimens in this research. The Young's moduli of the particle and the parallel bond were both 4.7 GPa, and the ratios of normal to shear stiffness of the particle and the parallel bond were both 2.5. The particle friction coefficient was 0.2. The mean value of the parallel bond normal strength (σ_n) and the mean value of the parallel-bond shear strength (τ_n) were, respectively, 32 MPa and 40 MPa, and the ratio of σ_n/τ_n was about 0.8.

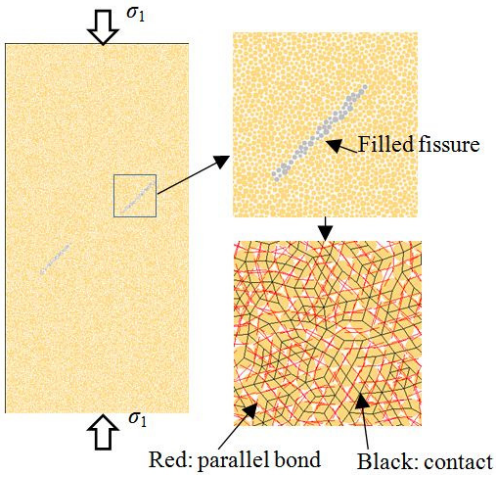

Fig. 10 Numerical specimen containing two non-coplanar filled fissures

Table 1 Micro parameters in PFC^{2D} of the intact specimen

Micro-parameters	Value
Young's modulus of particle, E_C / GPa	4.7
Young's modulus of parallel bond $\overline{E_c}$ / GPa	4.7
Ratio of normal to shear stiffness of particle, k_n / k_s	2.5
Ratio of normal to shear stiffness of parallel bond, $\overline{k_n} / \overline{k_s}$	2.5
Particle friction coefficient, μ	0.2
Parallel bond normal strength, σ_n / MPa	32±6
Parallel bond shear strength, τ_n / MPa	40±6

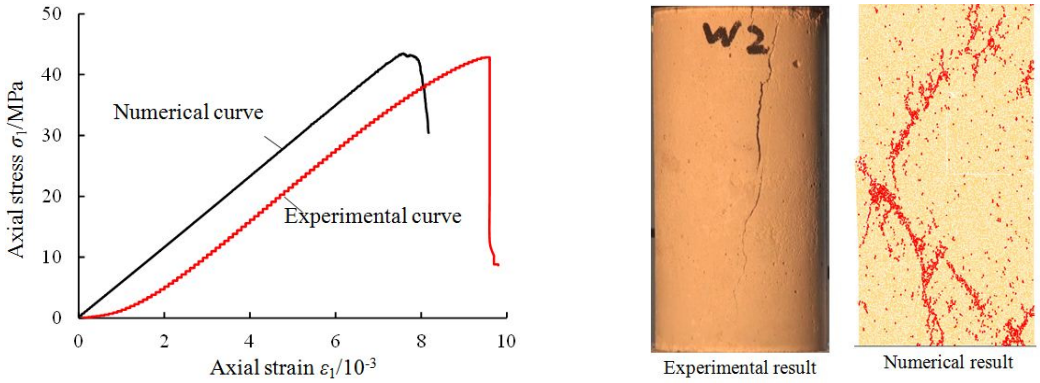

Fig. 11 Comparison of experimental and numerical results for intact rock-like material specimen under uniaxial compression

An external displacement was applied on the top and bottom of the wall in the axial direction. To ensure the specimen in a quasi-static equilibrium, the wall rate with 0.05 m/s was applied in this paper. PFC^{2D} will compute the critical time step first and assign a reasonable time step before each cycle. The time step is 4.91×10^{-8} s/step, this indicate that it requires 203665987.8 steps to move the specimen for 1mm.

The fissure's micro-parameters mainly affected the ultimate failure mode of flawed specimens, so through continuous adjustment, a group of micro-parameters were obtained. The normal stiffness of contact and parallel bond was 10^6 Pa, shear stiffness of contact and parallel bond was 10^3 Pa. The value of the parallel bond normal strength (σ_n) and the value of the parallel-bond shear strength (τ_n) were, respectively, 10^4 Pa and10^3 Pa.

Fig. 11 illustrated the comparison of experimental and numerical results of an intact rock-like material specimen under uniaxial compression. From Fig. 11 it can be seen that the numerically simulated curve under uniaxial compression agreed well with the experimental curve. The peak strength and elastic modulus of intact specimen obtained by numerical simulation were, respectively, 43.72 MPa and 5.75 GPa, which were approximately equal to those obtained by experiments (i.e., 43.49 MPa for peak strength and 5.84 GPa for elastic modulus). The numerical specimen also underwent typically axial splitting tensile failure, which approximated the experimental failure mode.

Fig. 12 showed the comparisons between experimental and numerical mechanical parameters

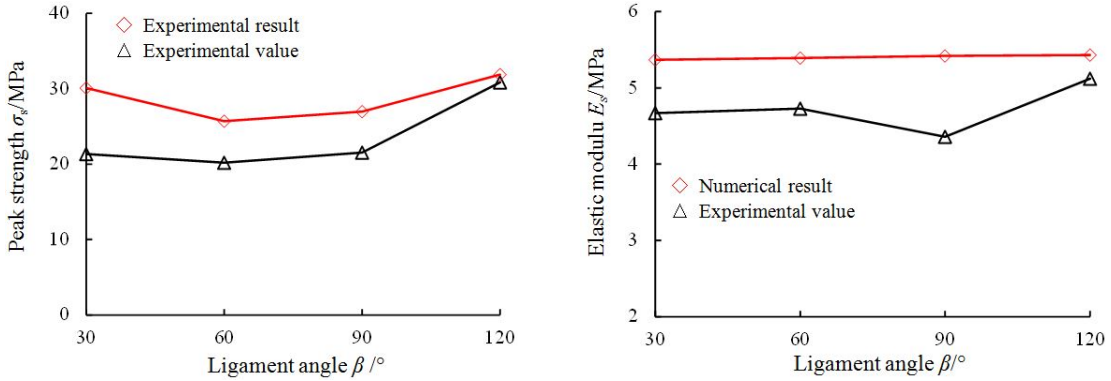

Fig. 12 Comparison of experimental and numerical mechanical parameters for specimens containing two filled fissures under uniaxial compression

for rock-like material specimens containing two non-coplanar filled fissures under uniaxial compression. From Fig. 12, it was clear that the peak strength of flawed specimens simulated by PFC^{2D} showed a similar trend with the increase of ligament angle. However, the simulated peak strength was greater than that obtained by experiments for the same ligament angle. From Fig. 12(b), it can be seen that numerical elastic modulus of flawed specimen was 1 GPa greater than that obtained by experiment for the same ligament angle. The above descriptions can be explained as follows. On the one hand, it is because the parallel bond model has lower UCS/TS ratio than the experiment. On the other hand, the particle size is larger than the grain size of the rock-like material, so the fissure created by numerical simulation is not the same as the experiment.

Fig. 13 illustrated the influences of ligament angle on the ultimate failure mode of rock-like material specimen containing two non-coplanar filled fissures under uniaxial compression using PFC^{2D} numerical simulation. In Fig. 13, the red points stood for the tensile crack, while blue points denoted the shear crack. Through comparisons with the experimental ultimate failure mode (see Fig. 5), we can see that the PFC^{2D} can be used to simulate the cracking characteristics of rock-like

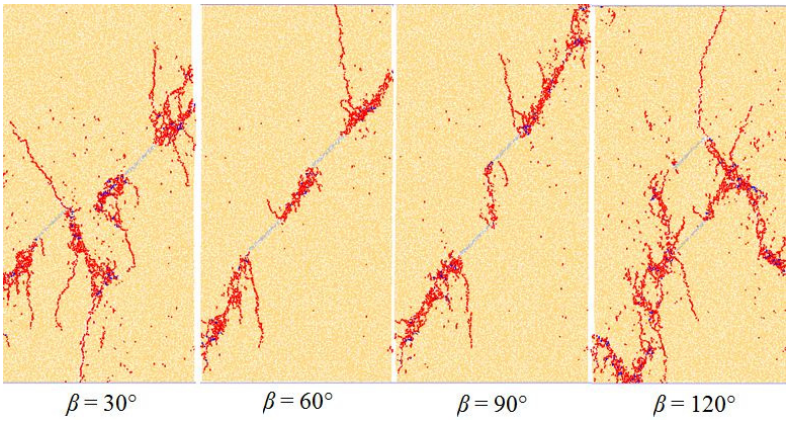

Fig. 13 Numerical results of ultimate failure modes of rock-like material specimen containing two non-coplanar filled fissures under uniaxial compression

materials. The ultimate failure modes of numerical specimens showed good consistency with those in experimental specimens.

4.2 Analysis of crack evolution mechanism

In order to analyze the crack evolution mechanism of rock-like material specimen containing two non-coplanar filled fissures under uniaxial compression, the specimens for $\beta = 60°$ and $\beta = 90°$ were chosen as examples, as was shown in Figs. 14~17. The letters in Fig. 15 corresponded to those in Figs. 16 and 17. Fig. 14 illustrates the parallel bond force fields of flawed specimens ($\beta = 60°$ and $\beta = 90°$) when the axial stress was 10 MPa. It should be noted that at this stress level, the first cracks did not initiate from the tip of fissures. In Fig. 14, the parallel bond forces were represented by the discrete straight line segments. Red color denoted tensile force, blue color

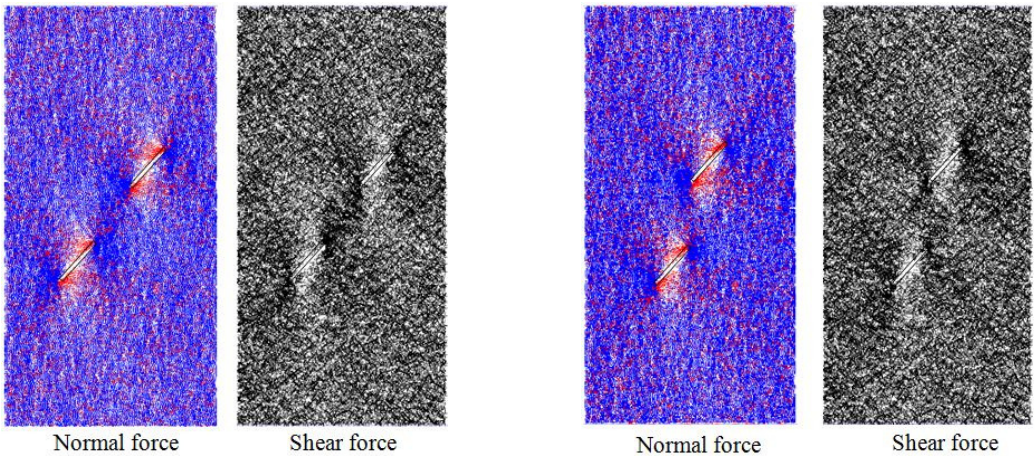

(a) $\beta = 60°$ (b) $\beta = 90°$

Fig. 14 Parallel bond force field of rock-like material specimen containing two non-coplanar filled force before the first crack initiation

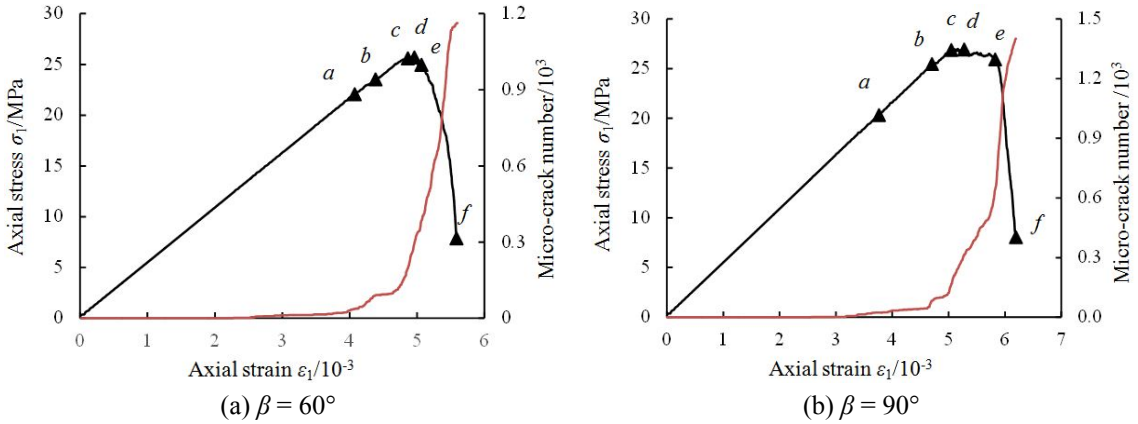

(a) $\beta = 60°$ (b) $\beta = 90°$

Fig. 15 Relation between axial stress-strain curve and micro-crack numbers of flawed specimen

denoted compressive force, while black color stood for shear force. Line thickness and orientation corresponded to force magnitude and direction, respectively. Form Fig. 14 it can be seen that the tensile forces mainly concentrated at left sides of the up tips and right sides of down tips, and compressive forces mainly concentrated at right sides of up tips and left sides of down tips. Shear force mainly concentrated at tip of fissures, but the region of shear forces concentrating in the flawed specimen for $\beta = 60°$ were larger than the flawed specimen for $\beta = 90°$.

Fig. 15 presented the relations between axial stress-strain curve and micro-crack number of rock-like material specimen containing two non-coplanar filled fissures ($\beta = 60°$ and $\beta = 90°$). From Fig. 15 we can see that more crack numbers occurred after the peak strength and cracks increased exponentially with the increase of axial deformation.

Fig. 16 illustrated crack evolution process and parallel bond force field of rock-like material specimen containing two non-coplanar filled fissures ($\beta = 60°$). In Fig. 16, the first row represented crack evolution, second row represented parallel bond normal force field and third row represented parallel bond shear force field, and the cracks were marked red and black in different rows in order to be observed more obviously. When specimen was loaded to the point *a* (σ_1 = 22.15 MPa, $\varepsilon_1 = 4.10\times10^{-3}$), wing cracks $1^{a\sim d}$ were initiated at tip of fissures. From Fig. 14(a) the red color crowded at tip of fissures, indicting the initiation of wing cracks $1^{a\sim d}$ at tip of fissures. When wing cracks initiated from the tip of fissures, the tensile stress concentration was released, the newly developed crack tips served as new tensile stress concentration region, and shear force crowded at tip of fissures more than Fig. 14(a).

As the axial stress increased to point *b* (σ_1 = 25.43 MPa, $\varepsilon_1 = 4.70\times10^{-3}$), crack number had a small rise, shear crack 2 was initiated from the inner tip of fissure ①, while wing crack $1^{a\sim d}$ propagated along the direction of axial stress. The shear force concentrated at tips of fissures more obviously, especially in the ligament region, and tensile force also crowded at tip of tensile cracks.

When the specimen was loaded to point *c* (σ_1 = 25.59 MPa, $\varepsilon_1 = 4.87\times10^{-3}$), crack numbers began to increase quickly with the increase of axial deformation, a few micro-cracks emanated in the ligament region of specimen, and Shear force also concentrated at the ligament region.

The continuous increase of axial deformation led the specimen to be loaded to peak strength point *d* (σ_1 = 25.7 MPa, $\varepsilon_1 = 4.98\times10^{-3}$), shear crack 3 initiated at the ligament region, and coalescence occurred quickly between fissure ① and fissure ②. At this time the concentration of shear force at ligament region was released, and the concentration of shear force region shifted to the outer tip of fissures. However, concentration of tensile force at tip of tensile crack 1^b and 1^c was released, but always crowded at tip of crack 1^a and 1^d. Due the coalescence between two fissures, the axial stress dropped quickly with the increase of axial deformation.

When the specimen dropped to point *e* (σ_1 = 22.12 MPa, $\varepsilon_1 = 5.25\times10^{-3}$), shear cracks 4^a and 4^b initiated at the outer tip of fissure ② and turning point of crack 1^d, respectively. The concentration of shear force near outer tip of fissures was more obvious than before. Tensile crack 1^a and 1^d appeared to propagate along the direction of axial stress, and tensile force also crowded at tip of crack 1^a and 1^d.

When the axial stress decreased to point *f* (σ_1 = 7.60 MPa, $\varepsilon_1 = 5.60\times10^{-3}$), shear crack $4^{a\sim b}$, and tensile crack 1^d propagated to the boundary of specimen, normal and shear force decreased obviously. At this time, the specimen failed completely in final macroscopic failure mode.

Compared with the crack evolution process and parallel bond force field of specimen with $\beta = 60°$ shown in Fig. 16, the crack evolution process and parallel bond force of rock-like specimen containing two non-coplanar filled fissures for $\beta = 90°$ were distinctly different, as was shown in Fig. 17. When the specimen was loaded to point *a* (σ_1 = 20.64 MPa, $\varepsilon_1 = 3.82\times10^{-3}$), wing cracks

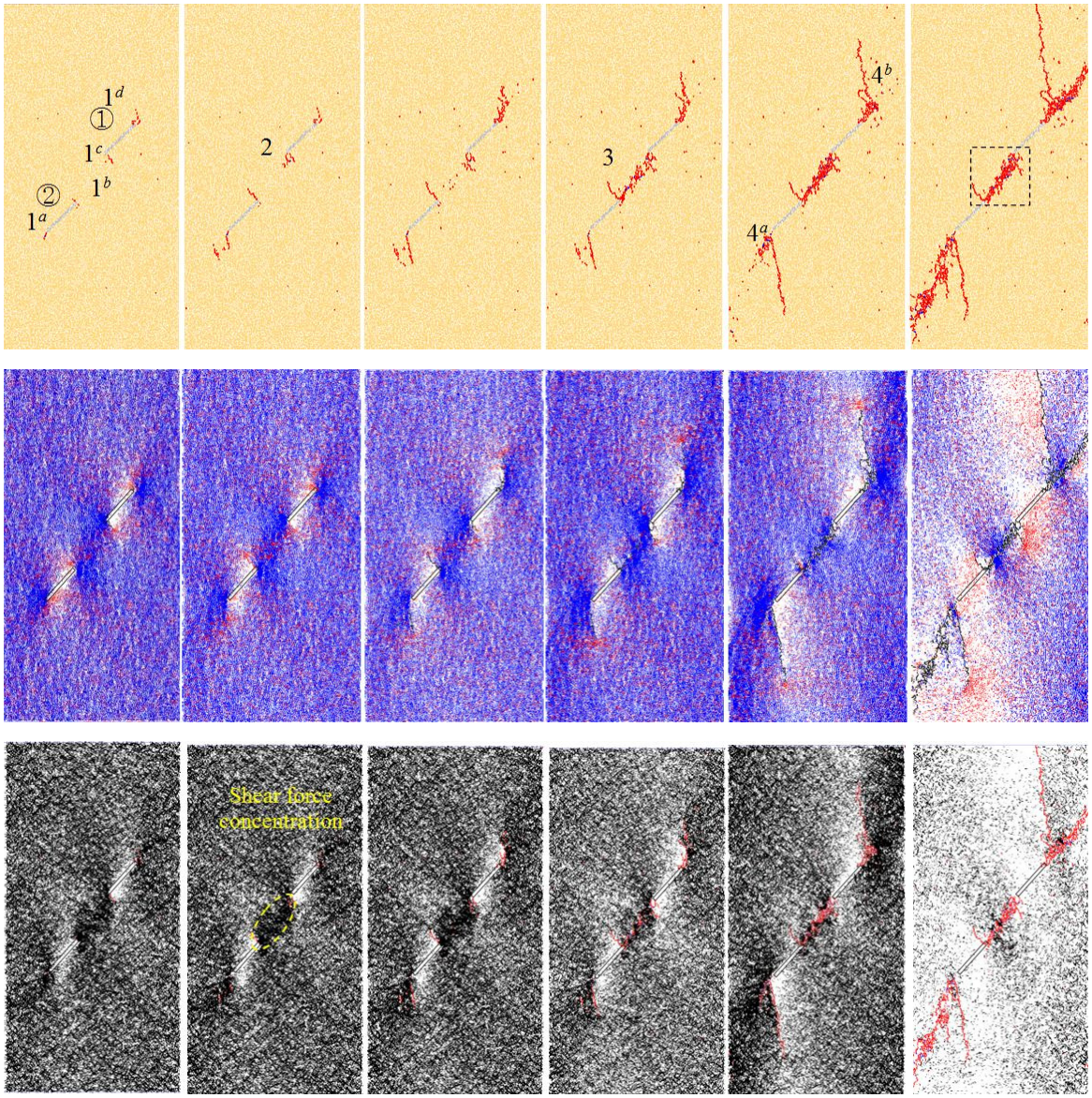

(a) σ_1 = 22.15 MPa, $\varepsilon_1 = 4.10\times10^{-3}$ (b) σ_1 = 23.58 MPa, $\varepsilon_1 = 4.40\times10^{-3}$ (c) σ_1 = 25.59 MPa, $\varepsilon_1 = 4.87\times10^{-3}$ (d) σ_1 = 25.7 MPa, $\varepsilon_1 = 4.98\times10^{-3}$ (e) σ_1 = 22.12 MPa, $\varepsilon_1 = 5.25\times10^{-3}$ (f) σ_1 = 7.60 MPa, $\varepsilon_1 = 5.60\times10^{-3}$

Fig. 16 Crack evolution process and parallel bond force field of rock-like material specimen containing two non-coplanar filled fissures (β = 60°)

$1^{a\sim d}$ initiated at tip of fissures, and crack number began to increased. From Fig. 16(b) the red color was crowded at tip of fissures, indicting the initiation of wing cracks $1^{a\sim d}$ at tip of fissures. When wing cracks initiated from the tip of fissures, the tensile stress concentration was released, the newly developed crack tips served as new tensile stress concentration region.

As the axial stress increased to point *b* (σ_1 =25.43 MPa, $\varepsilon_1 = 4.70\times10^{-3}$), wing crack propagated along the direction of axial stress. The axial stress had a small stress drop, and crack number had a

small rise, while the tensile force began to crowd at the ligament region.

The continuous increase of axial deformation led to the specimen being loaded to point *c* (σ_1 = 26.77 MPa, $\varepsilon_1 = 5.03\times10^{-3}$), tensile crack 2 emanated at the ligament region of specimen. At the same time, the tensile force concentration at ligament region was released, and shear force concentrated between the inner tip fissures and the tip of crack 2 and outer tip of fissures.

The continuous increase of axial deformation led to the specimen being loaded to peak strength

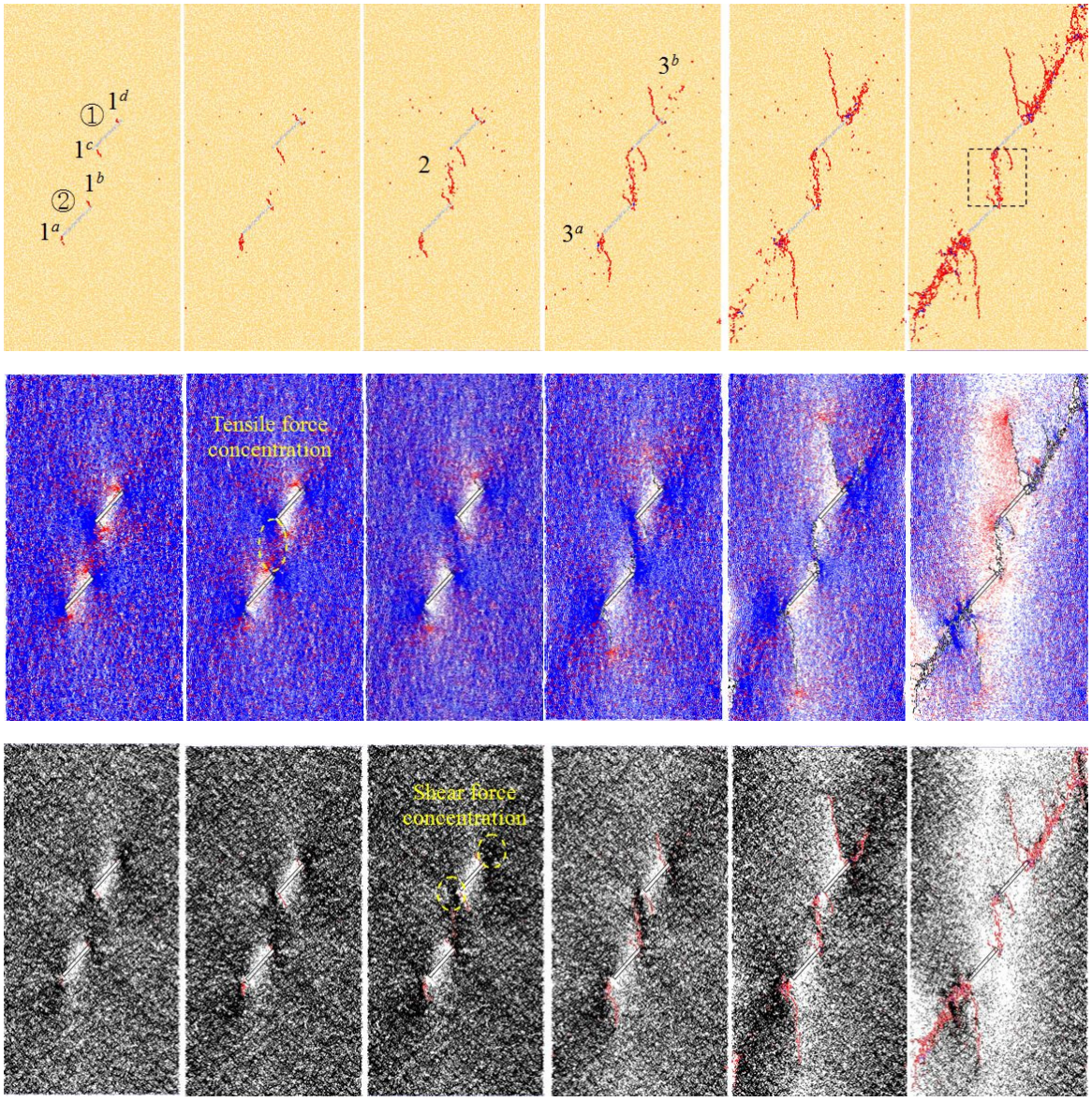

(a) $\sigma_1 = 20.64$ MPa, $\varepsilon_1 = 3.82\times10^{-3}$ (b) $\sigma_1 = 25.43$ MPa, $\varepsilon_1 = 4.70\times10^{-3}$ (c) $\sigma_1 = 26.77$ MPa, $\varepsilon_1 = 5.03\times10^{-3}$ (d) $\sigma_1 = 26.99$ MPa, $\varepsilon_1 = 5.22\times10^{-3}$ (e) $\sigma_1 = 25.93$ MPa, $\varepsilon_1 = 5.83\times10^{-3}$ (f) $\sigma_1 = 8.00$ MPa, $\varepsilon_1 = 6.19\times10^{-3}$

Fig. 17 Crack evolution process and parallel bond force field of rock-like material specimen containing two non-coplanar filled fissures ($\beta = 90°$)

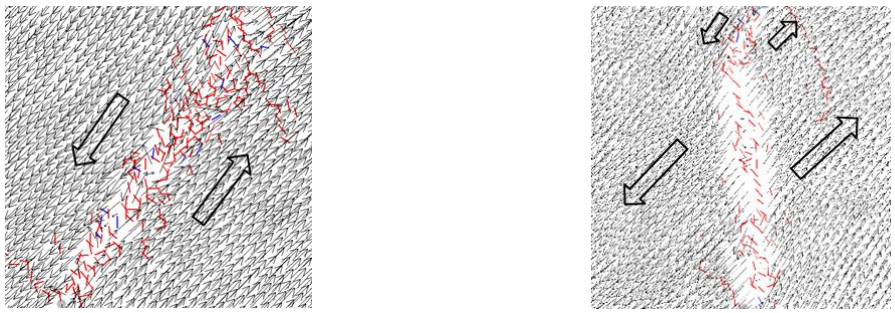

(a) $\beta = 60°$ (b) $\beta = 90°$

Fig. 18 The displacement vectors in ligament region with different ligament angle

point *d* (σ_1 = 26.99 MPa, $\varepsilon_1 = 5.22\times10^{-3}$), coalescence occurred between crack 2 and fissures due to the propagation of crack 2, and shear cracks 3^a and 3^b initiated at outer tip of fissures. The shear force concentration between crack 2 and the inner tip of fissures was released, but shear force also crowded near the outer tip of fissures. While the tensile forces concentrating at tip of crack 1^b and 1^c were released, tensile force also crowded at tip of crack 1^a and 1^d.

The axial stress did not drop obviously with the increase of axial deformation, although coalescence occurred at ligament region. When the specimen was loaded to point *e* (σ_1 = 25.93 MPa, $\varepsilon_1 = 5.83\times10^{-3}$), shear cracks 3^a and 3^b appeared parallel to the direction of fissures, and axial stress would drop quickly with increase axial deformation. Meanwhile, shear force also crowded near the tip of shear cracks.

When the axial stress decreased to point *f* (σ_1 = 8.00 MPa, $\varepsilon_1 = 6.19\times10^{-3}$), shear crack $3^{a\sim b}$ propagated to the boundary of specimen, normal and shear force decreased obviously. At this time, the specimen failed completely in final macroscopic failure mode.

Fig. 18 illustrated the displacement vectors in ligament region of flawed specimen with $\beta = 60°$ and $\beta = 90°$. From Fig. 18(a) we can see that the displacement vectors in sides of macro-crack had deflected direction and were parallel to macro-crack, and wider than that of tensile cracks (Zhang and Wong 2012), as was shown in Fig. 18(b). Combined with the Fig. 16, it can be seen that when $\beta = 60°$ coalescence occurred in the ligament region of flawed specimen with shear crack. From Fig. 18 (a) we can see that at middle region the displacement vectors in sides of macro-crack had deflected direction and were almost vertical to macro-crack, but near the tip of fissure, the displacement vectors in sides of crack had deflected direction and were parallel to macro-crack. Combined with the Fig. 17, it can be seen that tensile crack initiated at middle ligament region and coalescence occurred with shear crack. The result was similar to that obtained by Li (Li and Wong 2014). From the above analysis we can concluded that the macro-crack types were mainly identified by the parallel force distribution before crack initiation and displacement vectors after crack coalescence, but not the micro-crack type. The tensile micro-crack can occur even under the compression and shear state, due to the bending moment.

5. Conclusions

In this research, experiments and numerical simulations were adopted to investigate the effects of ligament angle on compressive strength and failure modes of rock-like material specimens

containing two non-coplanar filled fissures. Based on these experimental and numerical results, the following conclusions can be drawn.

(1) Rock-like material mixed with white cement, quartz sand and water used in this research has a great UCS/TS ratio, and it is a kind of brittle material which undergoes axial splitting failure. The experimental results show that the peak strength and elastic modulus of flawed specimens are lower than intact specimens. With the increase of ligament angle, the compressive strength decreases to a nadir at the ligament angle of 60°, before increasing to the maximum at the ligament angle of 120°, while the elastic modulus is not obviously related to the ligament angle.
(2) The shear coalescence mode easily occurred when $\alpha < \beta$, although having the same degree difference between the angle of ligament and fissure. When ligament angle was greater than 60°, the coalescence occurred before the peak strength point, but when ligament angle was less than 60°, the coalescence occurred after the peak strength point.
(3) PFC^{2D} was used to simulate the rock-like material containing filled fissures through reset property of ball in the fissures region. Peak strength, elastic modulus and ultimate failure were put forward to discriminate the rightness and reasonability of simulated results, and numerical simulation results showed good consistency with experimental results.
(4) By analyzing the crack evolution process and parallel bond force field of rock-like material specimen containing two non-coplanar filled fissures, we can conclude that the coalescence and propagation of crack mainly derived from parallel bond force, and the crack initiation and propagation also affected the distribution of parallel bond force. Finally, the displacement vectors in ligament region were used to identify the type of coalescence, and the results corresponded to that obtained by analyzing parallel bond force field.

Acknowledgments

This research was supported by the National Natural Science Foundation of Jiangsu Province for Distinguished Young Scholars (BK20150005) and the Fundamental Research Funds for the Central Universities (China University of Mining and Technology) (2014XT03). We also would like to express our sincere gratitude to the editor and two reviewers for their valuable comments, which have greatly improved this paper.

References

Bahaaddini, M., Hebblewhite, B.K. and Sharrock, G. (2013), "Numerical investigation of the effect of joint geometrical parameters on the mechanical properties of a non-persistent jointed rock mass under uniaxial compression", *Comput. Geotech.*, **49**(20), 2485-2488.

Bobet, A. and Einstein, H.H. (1998), "Fracture coalescence in rock-type materials under uniaxial and biaxial compression", *Int. J. Rock Mech. Min. Sci.*, **35**(7), 863-888.

Gehle, C. and Kutter, H.K. (2003), "Breakage and shear behavior of intermittent rock joints", *Int. J. Rock Mech. Min. Sci.*, **40**(5), 687-700.

Gerolymatou, E. and Triantafyllidis, T. (2016), "Shearing of materials with intermittent joints", *Rock Mech. Rock Eng.*, **49**(7), 2689-2700.

Haeri, H., Shahriar, K., Marji, M.F. and Moarefvand, P. (2014), "Experimental and numerical study of crack

propagation and coalescence in pre-cracked rock-like disks", *Int. J. Rock Mech. Min. Sci.*, **67**(4), 20-28.
Haeri, H., Khaloo, A. and Marji, M.F. (2015), "Experimental and numerical analysis of Brazilian discs with multiple parallel cracks", *Arab J. Geosci.*, **8**(8), 5897-5908.
Huang, D., Gu, D., Yang, C. and Fu, G. (2016), "Investigation on mechanical behaviors of sandstone with two preexisting flaws under triaxial compression", *Int. J. Rock Mech. Min. Sci.*, **49**(2), 1-25.
Janeiro, R.P. and Einstein, H.H. (2010), "Experimental study of the cracking behavior of specimens containing inclusions (under uniaxial compression)", *Int. J. Fract.*, **164** (1), 83-102.
Lee, H.W. and Jeon, S. (2011), "An experimental and numerical study of fracture coalescence in pre-cracked specimens under uniaxial compression", *Int. J. Solids Struct.*, **48**(6), 979-999.
Li, H.Q. and Wong, L.N.Y. (2014), "Numerical study on coalescence of pre-existing flaw pairs in rock-like material", *Rock Mech. Rock Eng.*, **47**(6), 2087-2210.
Lin, P., Robina, H.C., Wong, H.C. and Tang, C.A. (2015), "Experimental study of coalescence mechanisms and failure under uniaxial compression of granite containing multiple holes", *Int. J. Rock Mech. Min. Sci.*, **77**, 313-327.
Liu, H. and Zhang, L. (2015), "A compressive damage constitutive model for rock mass with a set of non-persistently closed joints under biaxial conditions", *Math. Problems Eng.*, **40**(11), 1-10.
Park, C.H. and Bobet, A. (2009), "Crack coalescence in specimens with open and closed flaws: A comparison", *Int. J. Rock Mech. Min. Sci.*, **46**(5), 819-829.
Prudencio, M. and Jan, M.V.S. (2007), "Strength and failure modes of rock mass models with non-persistent joints", *Int. J. Rock Mech. Min. Sci.*, **44**(6), 890-902.
Sagong, M. and Bobet, A. (2002), "Coalescence of multiple flaws in a rock-model material in uniaxial compression", *Int. J. Fract.*, **39**(2), 229-241.
Shen, B., Stephansson, O., Einstein, H.H. and Ghahreman, B. (1995), "Coalescence of fractures under shear stresses in experiments", *J. Geophys. Res. Solid Earth*, **100**(B4), 5975-5990.
Wang, L.H., Bai, J.L., Sun, X.S., Li, J.L., Tang, K.Y. and Deng, H.F. (2015), "The triaxial loading and unloading mechanical properties of jointed rock masses with different joint connectivities", *Chinese J. Rock Mech. Eng.*, **34**(12), 2500-2508.
Wong, R.H.C. and Chau, K.T. (1998), "Crack coalescence in a rock-like material containing two cracks", *Int. J. Rock Mech. Min. Sci.*, **35**(2), 147-164.
Wong, L.N.Y. and Einstein, H.H. (2009), "Systematic evaluation of cracking behavior in specimens containing single flaws under uniaxial compression", *Int. J. Rock Mech. Min. Sci.*, **46**(2), 239-249.
Xiao, T.L., Li, X.P. and Jia, S.P. (2015), "Failure characteristics of rock with two pre-existing transfixion cracks under triaxial compression", *Chinese J. Rock Mech. Eng.*, **34**(12), 2455-2462.
Xu, N.W., Dai, F., Wei, M.D. and Zhao, T. (2016), "Numerical observation of three-dimensional wing cracking of cracked chevron notched Brazilian disc rock specimen subjected to mixed mode loading", *Rock Mech. Rock Eng.*, **49**(1), 79-96.
Yang, S.Q. (2015), "An experimental study on fracture coalescence characteristics of brittle sandstone specimens combined various flaws", *Geomech. Eng.*, *Int. J.*, **8**(4), 541-557.
Yang, S.Q. and Jing, H.W. (2011), "Strength failure and crack coalescence behavior of brittle sandstone samples containing a single fissure under uniaxial compression", *Int. J. Fract.*, **168**(2), 227-250.
Yang, S.Q., Jiang, Y.Z., Xu, W.Y. and Chen, X.Q. (2008), "Experimental investigation on strength and failure behavior of pre-cracked marble under conventional triaxial compression", *Int. J. Solids Struct.*, **45**(17), 4796-4819.
Yang, S.Q., Tian, W.L., Huang, Y.H., Ranjith, P.G. and Ju, Y. (2016), "An experimental and numerical study on cracking behavior of brittle sandstone containing two non-coplanar fissures under uniaxial compression", *Rock Mech. Rock Eng.*, **49**(4), 1497-1515.
Yang, S.Q., Ranjith, P.G., Jing, H.W., Tian, W.L. and Ju, Y. (2017), "An experimental investigation on thermal damage and failure mechanical behavior of granite after exposure to different high temperature treatment", *Geothermics*, **65**, 180-197.
Zhang, X.P. and Wong, N.Y. (2012), "Cracking processes in rock-like material containing a single flaw under uniaxial compression: a numerical study based on parallel bonded-particle model approach", *Rock*

Mech. *Rock Eng*., **45**(5), 711-737.
Zhang, X.P. and Wong, L.N.Y. (2013), "Crack initiation, propagation and coalescence in rock-like material containing two flaws: a numerical study based on bonded-particle model approach", *Rock Mech*. *Rock Eng*., **46**(5), 1001-1021.
Zhang, B., Li, S.C., Zhang, D.F., Li, M.T. and Shao, D.L. (2012), "Uniaxial compression mechanical property test, fracture and damage analysis of similar material of jointed rock mass with filled cracks", *Rock Soil Mech*., **33**(6), 1647-1652.
Zhuang, X.Y., Chun, J.W. and Zhu, H.H. (2014), "A comparative study on unfilled and filled crack propagation for rock-like brittle material", *Theor*. *Appl*. *Fract*. *Mech*., **72**, 110-120.

CC